





RESEARCH ARTICLE | NOVEMBER 07 2024

Bubble fragmentation in turbulent flow and the potential implications of shear structures for bubbles formed by breaking waves

Ulrike Drähne ; Andrea Ducci ; Helen Czerski  



Physics of Fluids 36, 113329 (2024)

<https://doi.org/10.1063/5.0232421>



Articles You May Be Interested In

Bubble characteristics and turbulent dissipation rate in horizontal bubbly pipe flow

AIP Advances (February 2021)

Droplet size distributions in turbulent emulsions: Breakup criteria and surfactant effects from direct numerical simulations

J. Chem. Phys. (November 2013)

Droplet size distribution in homogeneous isotropic turbulence

Physics of Fluids (June 2012)



Physics of Fluids

Special Topics Open
for Submissions

[Learn More](#)



Bubble fragmentation in turbulent flow and the potential implications of shear structures for bubbles formed by breaking waves

Cite as: Phys. Fluids **36**, 113329 (2024); doi: 10.1063/5.0232421

Submitted: 7 August 2024 · Accepted: 12 October 2024 ·

Published Online: 7 November 2024



View Online



Export Citation



CrossMark

Ulrike Drähne,  Andrea Ducci,  and Helen Czferski^{a)} 

AFFILIATIONS

Department of Mechanical Engineering, University College London, Roberts Engineering Building, Torrington Place, London WC1E 7JE, United Kingdom

^{a)} Author to whom correspondence should be addressed: h.czferski@ucl.ac.uk

ABSTRACT

Large bubbles (1–5 mm radius) are important in a wide range of situations, including air-sea gas transfer, aerosol production as they burst at water surfaces, and the aeration of liquids in bioreactors and other industrial processes. When rising through turbulent flow, these bubbles are commonly distorted and may fragment to form daughter bubbles if their radius exceeds the Hinze scale (at which the restoring force due to surface tension is equal to the forces causing bubble distortion). Here, we present the results of laboratory experiments with fragmentation resulting from bubbles rising through a sheared and turbulent flow. The effects of water temperature, surface tension, local shear rate, and viscous dissipation rate of turbulent kinetic energy were assessed. Passive acoustical methods produce robust measurements of bubble fragmentation processes, allowing for rapid data collection to generate large data sets. In our experiments, even for bubbles very close to the Hinze scale, the dominant fragmentation mechanism is the capillary-driven fragmentation of elongated bubble filaments. The probability distribution of daughter bubble sizes from a single fragmentation event was independent of temperature, surface tension, and rate of viscous dissipation of turbulent kinetic energy. The overwhelming majority of fragmentation events resulted in one very large and one very small bubble, even for Hinze-scale parent bubbles and low Weber numbers ($We < 5.3$). Our results suggest that in a turbulent flow, there may be a link between the shear induced by large scale structures and the size of the smallest bubbles produced underneath a breaking wave.

© 2024 Author(s). All article content, except where otherwise noted, is licensed under a Creative Commons Attribution (CC BY) license (<https://creativecommons.org/licenses/by/4.0/>). <https://doi.org/10.1063/5.0232421>

I. INTRODUCTION

The bubbles formed by breaking waves at the ocean surface are important for air-sea gas transfer (Deike, 2022; Deike and Melville, 2018; and Wanninkhof, 2014), aerosol production (Berny *et al.*, 2020; de Leeuw *et al.*, 2011), and upper ocean optical (Salisbury *et al.*, 2013; Stramski and Tegowski, 2001) and acoustical (Chua *et al.*, 2021; Deane, 2016; and Deane and Stokes, 2010) properties. Bubbles are formed as air is entrained at the breaking wave crest and then may be further fragmented by subsurface turbulence in the first second or so after formation. Deane and Stokes (2002) observed that the size distribution within the crest during active breaking has two distinct slopes: a slope of $-10/3$ for larger bubbles, which is consistent with a bubble fragmentation cascade due to the turbulent flow, as set out in Garrett *et al.* (2000) and elaborated on in Rivière *et al.*, (2022), and a slope of $-3/2$ for smaller bubbles. The bubble radius at the slope break is the Hinze scale: the critical radius at which surface tension can stabilize

the bubble against the shear forces associated with the turbulent flow. The rate of viscous dissipation of turbulent kinetic energy underneath breaking waves is typically $2\text{--}30 \text{ W kg}^{-1}$ (Deane, 2012), corresponding to a Kolmogorov length scale of $1.4\text{--}2.7 \times 10^{-5} \text{ m}$, while the Hinze scale is relatively insensitive to the turbulent dissipation rate, varying from approximately 0.7–2 mm in radius over that range. Bubbles larger than the Hinze scale are thought to be particularly important for the air-sea transfer of carbon dioxide, even though they are short-lived, so there is considerable interest in their formation processes, along with the depth reached and time spent submerged.

Although the outline processes of bubble production in breaking waves have been established, there are still uncertainties which limit the ability of models to incorporate full process details and to predict the influence of those bubble populations. This is particularly apparent in the first few seconds after wave breaking, and consequently there are ongoing efforts to better understand the process of bubble

fragmentation in turbulence. Turbulent fragmentation is also significant for other applications, for example bubble breakup in stirred bioreactors that can induce cell damage (Buffo, 2016), and droplet breakup in multiphase flows (Rosti *et al.*, 2019).

Recent experimental and modeling work has significantly advanced the understanding of turbulent fragmentation. Much of this is framed in terms of the Weber number, which can be interpreted in terms of a ratio between the capillary and inertial time scales. It is defined for a bubble in isotropic homogenous turbulence (Rivière *et al.*, 2021) as

$$We = \frac{2\rho_W \varepsilon^{\frac{2}{3}} d_0^{\frac{5}{3}}}{\sigma}, \quad (1)$$

where ρ_W is water density, ε is the turbulent kinetic energy viscous dissipation rate, d_0 is bubble diameter, and σ is the air–water surface tension. The Hinze scale is the bubble radius at the critical Weber number We_C : the largest bubble size that will deform but not fragment at a specified level of turbulence (although these are stochastic processes, so this is a soft limit). Values of We_C in breaking wave crests are found experimentally to be between 0.7 and 5, and Rivière *et al.*, (2021) find $We_C \approx 3$ using direct numerical methods. Qi *et al.* (2022) question the use of the Weber number as the sole criterion for fragmentation, on the basis that it does not account sufficiently for the scales of the turbulent eddies involved, and propose the use of two dimensionless numbers so that both bubble and eddy sizes can be represented. Rivière *et al.*, (2021) carried out numerical simulations of turbulent breakup, highlighting the different characteristics of bubble fragmentation for parent bubbles that were close to the Hinze scale and those much larger than it. Bubbles close to the Hinze scale were seen to fragment into 2 or 3 daughter bubbles, which were relatively similar in size while multiple daughter bubbles with sizes far smaller than the parent bubble were produced as elongated filaments of gas became unstable. These studies highlight the complexity of the processes involved and the need for robust experimental evidence to constrain models.

The motivation for understanding the fragmentation process is the desire for a model that can make robust predictions of the bubble size distributions produced in different physical conditions in the open ocean. One essential component is the size distribution of the daughter bubbles formed by a fragmentation event and its dependence on parent bubble radius, water characteristics, and the flow field. Qi *et al.* (2020) suggest that over relatively long time periods, the $-10/3$ slope for bubbles larger than the Hinze scale forms irrespective of the daughter bubble size distribution but concluded that the time needed to reach that state varies so there is still a need to predict the fragmentation outcome. Several models have been proposed to predict the daughter bubble size distribution formed by fragmentation. As Qi *et al.*, (2020) set out, they vary widely in their predictions because there are many physical mechanisms that could dominate the process and each model chooses to prioritize these differently. Qi *et al.* (2020) state that they broadly fall into three categories: bell-shaped (e.g., (Martínez-Bazán *et al.*, 1999)), U-shaped (e.g., (Tsouris and Tavlarides, 1994)), or M-shaped (Wang *et al.*, 2003)). Some experimental evidence is available to constrain the models, but it tends to be indirect (using, for example, the overall bubble population outcome (Martínez-Bazán *et al.*, 1999)) or limited by the difficulty of measuring breakup processes accurately. Extensive reviews of these models can be found in Qi *et al.*, 2020, 2022; Rivière *et al.*, 2021.

More recent work (Rivière *et al.*, 2022) has produced a convincing explanation for the $-3/2$ slope of sub-Hinze scale bubbles in the initial bubble population. Their numerical models suggest that two processes are at work: a “breakup” mechanism, which produces two approximately equally sized bubbles and is controlled by bubble interaction with turbulent eddies, and a “splitting” mechanism that acts on bubbles much larger than the Hinze scale and causes the production of much smaller sub-Hinze scale daughter bubbles as narrow gas filaments fragment. The parameters controlling the exact size and outcome of the splitting process are still uncertain.

In this work, we address the relative lack of robust experimental data to constrain models of the daughter bubble size distribution. The existing experimental measurements mostly rely on high-speed photography followed by image processing, sometimes from multiple directions (Yinghe Qi *et al.*, 2020), which is a computationally expensive process. Our study takes a different approach. It is well-established that at the moment of bubble formation (any circumstance that involves an underwater pocket of gas breaking away from either another gas pocket or a large gas reservoir like the atmosphere), the new bubble will emit an acoustical pulse at its natural frequency (Czerski and Deane, 2010; Deane and Czerski, 2008). At the moment of formation, the recently broken neck of the bubble has a very small radius of curvature and surface tension will cause a rapid shape change as the bubble returns to an equilibrium shape. This generates compression of the gas inside the bubble on a timescale, which is less than the natural period of oscillation of the bubble, and the bubble is, therefore, stimulated into volume mode oscillations. The acoustic pulse is a decaying sinusoid with a frequency that depends predominantly on the bubble radius. The oscillation frequency f of the bubble is inversely proportional to the bubble radius R according to the Minnaert equation (Minnaert, 1933)

$$R = \frac{1}{2\pi f} \cdot \sqrt{\frac{3 \cdot \kappa \cdot p_0}{\rho}}, \quad (2)$$

with $\kappa = 1.4$ denoting the ratio of the specific heat capacity of air at constant pressure to the specific heat capacity of air at constant volume (Leroy *et al.*, 2002), $p_0 = 10^5$ Pa being the atmospheric pressure, and ρ denoting water density. This simple equation applies to individual bubbles of an ideal gas undergoing a radial oscillation at their natural frequency and can be derived by treating the bubble as a mass-spring system. Surface tension and viscous attenuation are ignored (a valid assumption for air bubbles in water of the radii considered here). The sound produced has a wavelength far larger than the size of the bubble, and therefore, this is primarily a volume oscillation—the “breathing mode”—so small asymmetries in the bubble shape make a negligible difference to the radiated sound. For bubbles of a few millimeters in radius, the Minnaert equation produces very accurate results and is, therefore, appropriate for this study.

When bubbles fragment in the turbulent flow, the two new daughter bubbles oscillate as a coupled system (Czerski and Deane, 2011) and their sizes can be deduced by fitting superimposed decaying sinusoids to the signal. The extreme shape distortions at the moment of breakup do not affect the inferred sizes because the bubble size is far less than the wavelength of the sound (the wavelength is 1.45 m for a 3.2 mm radius bubble), and so only the volume oscillation is significant. Consequently, this acoustical method provides a more accurate measure of effective radius than photography, which can only provide

an approximate size for highly distorted bubbles viewed from one side only. The other major advantage of this system is that it provides accurate sizes for the two daughter bubbles with a far simpler method than is used for the photographic studies. This permits a very large number of tests to be conducted, providing very robust statistics.

Characterization of the flow field is important for any fragmentation study. However, it is challenging to measure the turbulence inside the breaking wave crest because bubbles interfere with methods based on particle tracking, and because of the intermittent, spatially variable and short-lived nature of the active period of breaking. The most direct measurements to date were carried out by [Deane *et al.* \(2016\)](#), who used calibrated measurements of the light from bioluminescent dinoflagellates to infer shear rates inside laboratory breaking wave crests. They found that average turbulent intensity saturated at around $0.5\text{--}1.2\text{ W kg}^{-1}$ and was independent of the overall loss of energy from the breaking crest. The probability of seeing high local values in their experiments dropped off very sharply above 10 W kg^{-1} . Here, we characterize the flow field using Particle Image Velocimetry (PIV) ([Ducci and Weheliye, 2014](#)) before bubbles are introduced (i.e., single phase flow) and subsequently use high speed photography to assess where in the flow field bubbles are most likely to fragment.

We measured the daughter bubble size distribution produced by fragmentation in the turbulent sheared flow produced by two slightly offset opposing jets, for a range of temperature conditions and surface tension values. In the case of multiple fragmentations, we consider the first fragmentation only, which provides a measure against which models can be tested. Temperature predominantly affects water viscosity, which is not a critical parameter in most models. However, [Salter *et al.* \(2014\)](#) observed significant differences in the bubbles produced at different temperatures from a plunging jet, particularly at temperatures below $11\text{ }^{\circ}\text{C}$, which justifies our experimental investigation here. Surface tension will influence the Weber number and is of particular interest because natural surfactants at the ocean surface can vary considerably with location ([Wurl *et al.*, 2011](#)).

II. MATERIALS AND METHODS

A. Experimental setup for bubble fragmentation

Two slightly offset colliding jets were used to generate a high shear turbulent flow. The setup is shown in [Fig. 1](#). The measurement tank was $31.0\text{ cm} \times 31.0\text{ cm} \times 51.0\text{ cm}$ and the smaller feeder tank

measured $26.6\text{ cm} \times 26.6\text{ cm} \times 33.6\text{ cm}$. Individual bubbles were generated at a nozzle at the bottom of the tank and rose into the high shear region.

Water was pumped from the feeder tank into the measurement tank using a Cole Parmer high-performance peristaltic pump (model number: 77600-62) rotating at a pump speed, which was varied from 30 to 50 rpm. The water entered the measurement tank through two L-shaped glass tubes offset vertically by 1 cm, generating a local region of high shear and turbulence (Reynolds number $Re \sim 10^3\text{--}10^4$). As bubbles rose through this shear region fragmentation frequently, but not always, occurred.

The undisturbed water depth was approximately 30 cm in the measurement tank. While the pump was running, the water level in the measurement tank increased due to the additional water input through the glass tubes. To close the flow cycle, a 3 cm diameter pipe allowed water to siphon back into the feeder tank at a rate dependent on the pressure head. All components were mechanically isolated as much as possible to reduce the propagation of acoustical pump noise to the hydrophone. Tap water was used for all experiments performed in this study and was continuously filtered for half an hour by a water treatment unit (UV sanitizer and particulate filtration), before every experimental run.

The bubbles were generated by pumping air through a thin glass tube near the tank base at a manually controlled flow rate. Bubbles were generated at a rate of one bubble every 1.2–2.6 s to ensure that each bubble was independent of preceding and subsequent bubbles.

A hydrophone manufactured by Reson (model number: TC4013-1) was located at the same height and at a horizontal distance of approximately 3 cm from the center of the sheared region, to record the sound produced by the bubbles during the fragmentation process. The acoustical signal was amplified using a Reson VP2000 hydrophone pre-amplifier (model EC6081).

Experiments were performed at six water temperatures between 3 and $30\text{ }^{\circ}\text{C}$ and at a pump speed of 50 rpm. Temperature was controlled by using either two commercially available aquarium heaters or by placing ice cubes in the feeder tank. Triton-X-100 was used to decrease the water surface tension for two additional cases at $22\text{ }^{\circ}\text{C}$, (i) surface tension of 0.051 N/m (2 ml of Triton-X-100 in 40 l of water), 50 rpm and (ii) 0.032 N/m (24 ml of Triton-X-100 in 40 l), 30 rpm. The water surface tension was measured using the capillary rise method.

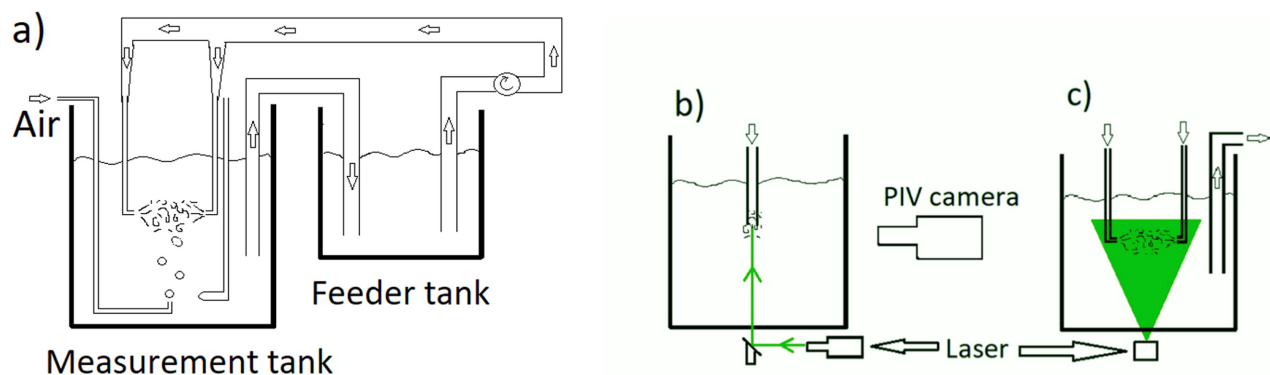


FIG. 1. (a) Experimental setup for bubble fragmentation experiments, (b) experimental setup of the measurement tank for PIV measurements, side view, and (c) front view, showing the laser sheet in green.

B. Experimental setup for PIV measurements

The PIV analysis of the flow was carried out independently of the fragmentation experiments. A vertical sheet of laser light was projected into the main tank from underneath in order to track water flow in the plane of the flow tubes, as shown in Figs. 1(b) and 1(c). The cylindrical lens widened the horizontal laser beam to a fan-pattern, which was reflected by the 45° mirror upwards into the measurement tank so that it bisected both flow tubes. The water was seeded with silver coated micro-spheres with a high refractive index and a diameter of 10 μm. The laser was a Class 3 b continuous diode laser manufactured by Laserglow Technology, emitting 532 nm green light with an average power output of 447 mW.

PIV flow tests were performed at pump speeds of 30, 40, and 50 rpm. For each experimental run, 1000 camera images were recorded at 1 620 frames per second, an exposure time of 614 μs, and a gain of −3 dB. Pairs of consecutive images were analyzed for particle displacement using the open source software *JPIV*, resulting in 999 processed images for each run. The interrogation region was 128 pixels across (34 mm) with a window size of 16 pixels (4.23 mm). Image pre-processing comprised of a multipass correlation analysis, setting invalid velocity vectors to zero, and a median filter. Post-processing was carried out with Matlab.

C. High speed photography

The location of bubble fragmentation in the flow field was determined for a small subset of experiments to gain a better understanding of how and under which conditions bubble fragmentation occurs. A Phantom VEO 710 L high-speed camera was used to capture at least 10 seconds of video for each event with a frame rate of 8 300 fps. The pixel coordinates of the narrowest point of the bubble neck between daughter bubbles were noted manually from the frame just prior to fragmentation. In the case of multiple fragmentations, only the first event was recorded. For each experimental condition, the fragmentation location of 100 bubbles was determined. The high speed video was used to manually assign each event into one of three categories:

- 1 Solo binary fragmentation: parent bubble fragments into exactly two daughter bubbles; none of the daughter bubbles fragments again.
- 2 Fragmentation cascade: parent bubble fragments and either one or both daughter bubbles fragment at least once more within the 10 s video.
- 3 Sequential fragmentation (a subset of case 2): a parent bubble produces successive tiny daughter bubbles as part of the same event.

We note that all of these cases are binary fragmentation events, even if successive events are not independent of each other. The parent bubble was never observed to break up into a cloud of daughter bubbles in a single event, although successive events could occur within a few milliseconds. With two exceptions, all the high speed photography data for each condition were collected on the same day in an uninterrupted run. The exceptions were the 22 °C case, which ran over two days and the 11 °C case, which included one 11 min break to re-adjust the water temperature. Figure 2 shows extracted video frames from two types of fragmentation.

III. DATA PROCESSING

A. Acoustical analysis

The acoustical analysis described here follows the previously established method of fitting decaying sinusoids to the signal from each bubble fragmentation event (Czerski and Deane, 2011). Sound pressure was normalized to 1 m distance using the following equation:

$$\frac{p_2}{p_1} = \frac{r_1}{r_2}. \quad (3)$$

Here, p_1 is the sound pressure of the measured signal, p_2 is the sound pressure at 1 m distance, $r_1 = 0.03$ m (distance between bubble and hydrophone), and $r_2 = 1$ m.

Each individual event started with a rapid rise in acoustic pressure, and the signal used for analysis was a 10 ms acoustical segment starting at the maximum identified amplitude. A Fast Fourier Transform was used to estimate the dominant two frequencies, and these were used as the initial parameters for the fitting algorithm. The signals were then fitted using an 8-parameter fit representing the sum of two damped harmonic oscillators,

$$A = A_1 \cdot \sin(\omega_1 t + \phi_1) \cdot e^{-\frac{1}{2}\delta_1 \omega_1 t} + A_2 \cdot \sin(\omega_2 t + \phi_2) \cdot e^{-\frac{1}{2}\delta_2 \omega_2 t}, \quad (4)$$

$A_{1,2}$ is the pressure amplitude in [Pa], $\omega_{1,2}$ is the angular frequency [rad/s], t is time in [s], $\phi_{1,2}$ is the phase shift, and $\delta_{1,2}$ is the damping constant. Subscript indices refer to each daughter bubble. Bubble frequency was later used to calculate daughter bubble radii. Figure 3 shows an example of a typical acoustic signal emitted during a fragmentation event overlaid with the fitted model.

Every fit was assessed to check that the fit outputs were within physically plausible bubble parameter ranges. Occasional spurious signals due to bubbles colliding with the glass tubes and causing the tubes to ring were easily identified by their low damping constants (below 0.04) and narrow frequency range, and were excluded. After applying these quality control criteria, the total number of reliable fragmentation events was 1 061, 394, 354, 1374, 953, and 366 events at 3, 5, 8, 11, 22, and 30 °C (a total of 4502 events). All surface tension experiments were carried out at 22 °C (1470 and 1643 fragmentation events for surface tension values of 0.032 and 0.051, respectively).

The fragmentation rate was monitored by manually checking 600–1 200 events for each condition. The original size of the parent bubble was determined from the sum of the daughter bubble volumes and was found to be 3.13 ± 0.12 mm, 3.32 ± 0.16 mm, 3.22 ± 0.17 mm, and 3.04 ± 0.10 mm at 3, 11, 22, and 30 °C, respectively. When the surface tension was varied, the parent bubble radius was 2.80 ± 0.33 mm at both 0.032 N/m and 0.051 N/m (all at 22 °C). The fragmentation rates were 61.3%, 66.3%, 36.0%, 45.0%, and 54.1% at 3, 5, 8, 11, and 30 °C, respectively. The fragmentation rate was 71.9% and 67.3% at 0.032 N/m and 0.051 N/m, respectively.

B. PIV analysis

The 2D mean velocity field was calculated from the particle displacement as the average over 999 time steps. We define the horizontal velocity component u along the x-direction and the vertical velocity component v along the y-direction. The spatial resolution of the current PIV measurement, $\Delta = 1.4$ mm, does not allow us to resolve the

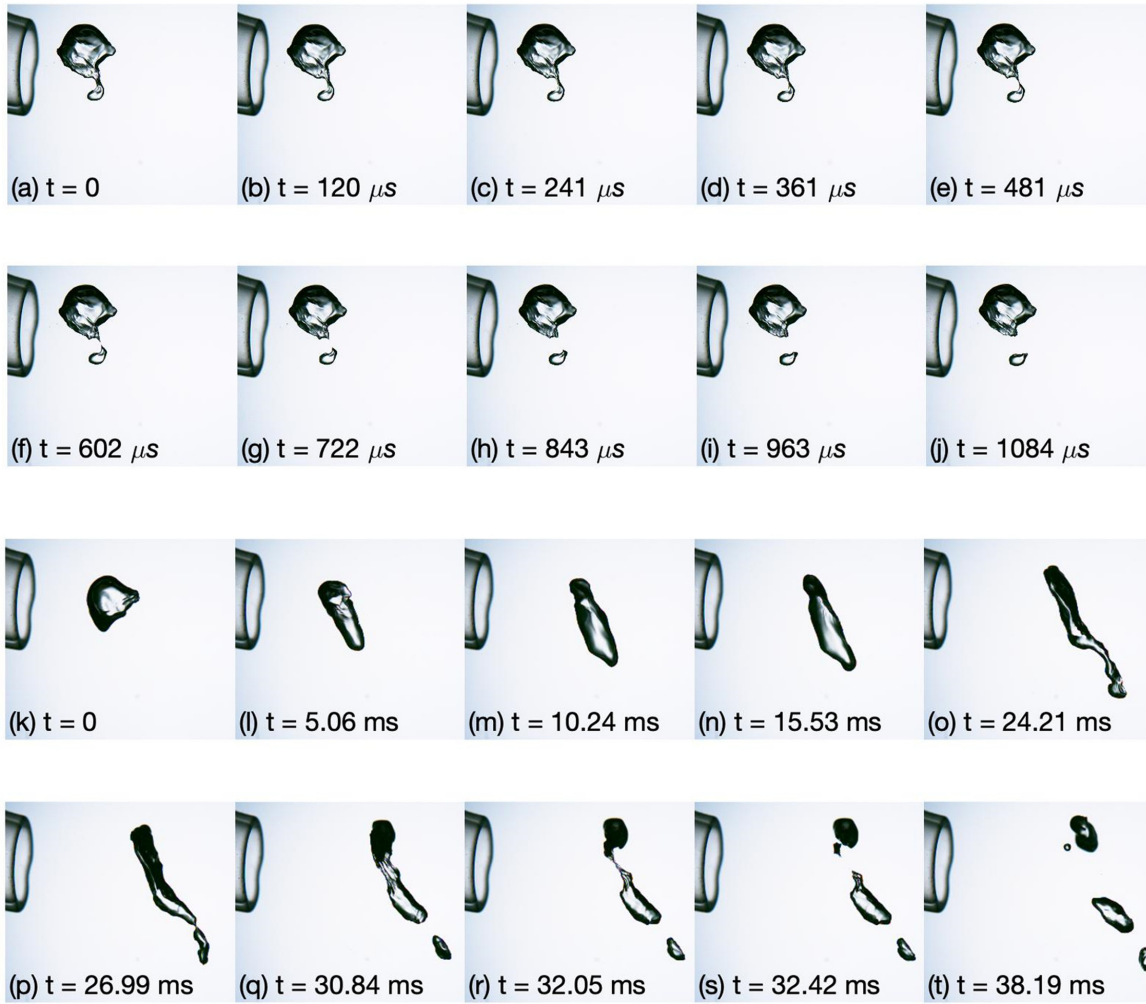


FIG. 2. High speed camera images of two fragmentation events at 22 °C, with a pump speed of 50 rpm. The Weber number is 5.3, and the ratio of the parent bubble size to the Hinze scale is 1.4. The field of view shown is 3.9×3.3 cm in all cases. (a)–(j) Solo binary fragmentation with a resulting volume split ratio of 0.96:0.04. (k)–(t) A fragmentation cascade that is not a sequential fragmentation.

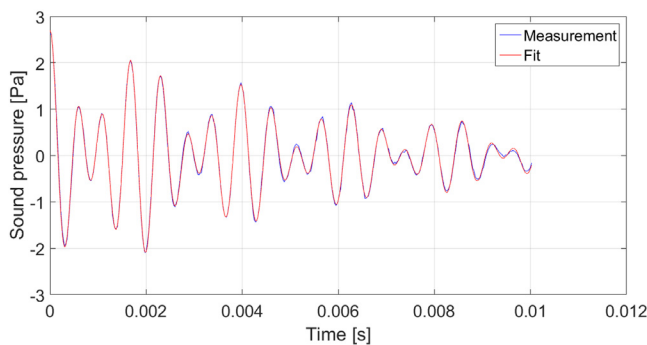


FIG. 3. Measured acoustic signal (blue) emitted during a fragmentation event at 22 °C and fit (red). Measured and fitted signals are in very good agreement and are often hard to distinguish.

dissipative length scale and, therefore, provide a direct measurement of the full viscous dissipation rate of turbulent kinetic energy. As a consequence, a Large eddy Particle Image Velocimetry, LePIV, approach was used to estimate the full dissipation rate. The eddy viscosity model (i.e., a Smagorinski model) is used to estimate the sub grid shear stress tensor, τ_{ij} (Sheng *et al.*, 2000). The notation of the works of Vejražka *et al.* (2018) and de Jong *et al.* (2008) has been used here, where the PIV resolved velocities (i.e., measured velocity) are denoted by a hat symbol. In this case, the resolved instantaneous strain rate tensor, \hat{S}_{ij} , is defined as

$$\hat{S}_{ij} = \frac{1}{2} \left(\frac{\partial \hat{u}_i}{\partial x_j} + \frac{\partial \hat{u}_j}{\partial x_i} \right). \quad (5)$$

When using the eddy viscosity model, the dissipation rate can be calculated according to the following equation:

$$\varepsilon = 2C_s^2 \Delta^2 \left\langle \sqrt{\hat{S}_{kl} \hat{S}_{kl} \hat{S}_{ij} \hat{S}_{ij}} \right\rangle, \quad (6)$$

$C_s = 0.17$ is the Smagorinski constant [see [Vejražka et al. \(2018\)](#) and [de Jong et al. \(2008\)](#)] and Δ denotes “filter” size, which is equal to the spatial resolution of the PIV measurements (i.e., equivalent to the “resolved scale” in large eddy simulations). Broken brackets indicate time averaged values. Since we used 2D PIV measurements, only four of the nine strain rate tensor elements can be calculated directly. Therefore, the dot products \hat{S}_{kl} and \hat{S}_{ij} are each approximated by ([Vejražka et al., 2018](#))

$$\hat{S}_{ij} \hat{S}_{ij} \approx 2 \left(\frac{\partial \hat{u}}{\partial x} \right)^2 + 2 \left(\frac{\partial \hat{w}}{\partial z} \right)^2 + 2 \frac{\partial \hat{u}}{\partial x} \frac{\partial \hat{w}}{\partial z} + \frac{3}{2} \left(\frac{\partial \hat{u}}{\partial z} + \frac{\partial \hat{w}}{\partial x} \right)^2. \quad (7)$$

The maximum shear rate we use here is not the maximum numerical value of the shear rate at any time, but rather a measure of the relative shear rate calculated following the approach by [Rodríguez \(2017\)](#) as shown in Eq. (5). After calculating the 2D spatial gradients using the corresponding mean-subtracted velocity components, the 2D strain rate tensor \hat{S} defined as

$$\hat{S} = \begin{bmatrix} \frac{\partial \hat{u}}{\partial x} & \frac{1}{2} \left(\frac{\partial \hat{u}}{\partial y} + \frac{\partial \hat{v}}{\partial x} \right) \\ \frac{1}{2} \left(\frac{\partial \hat{u}}{\partial y} + \frac{\partial \hat{v}}{\partial x} \right) & \frac{\partial \hat{v}}{\partial y} \end{bmatrix}, \quad (8)$$

was calculated at every point. The strain rate tensor includes local rates of shear, compression, and stretching. Next, the eigenvalues \hat{S}_1 and \hat{S}_2 of the strain rate tensor were determined, and the third eigenvalue, \hat{S}_3 , was calculated from the continuity equation. Positive eigenvalues indicate stretching, while negative eigenvalues are associated with local compression ([Rodríguez, 2017](#)). The maximum shear rate $\dot{\gamma}_{max}$ was then determined at every point as the maximum difference between any of the three eigenvalues,

$$\dot{\gamma}_{max} = \frac{(S_i - S_j)_{max}}{2}. \quad (9)$$

Here, i and j were chosen so that the difference— $S_i - S_j$ —between the individual eigenvalues was maximized. The value for maximum shear rate that we use here is therefore the maximum shear rate in any direction at that location, averaged over time.

IV. RESULTS

A. Effects of temperature on fragmentation

We use the volume split ratio to assess the fragmentation outcome: the probability distribution of the daughter bubble volumes as a fraction of their parent bubble volume. The distribution is necessarily symmetrical because each daughter bubble is one of a pair. Volumes for the daughter bubbles were calculated using the fitted frequency from Eq. (4), converted into radius using Eq. (2). [Figure 5\(e\)](#) shows a probability density function of the volume split ratios for all temperatures (3–30 °C), no added surfactants, and a pump speed of 50 rpm.

For all water temperatures, the normalized volume split ratio has a very similar distribution: a “U” shape with a minimum for similarly sized bubbles and two maxima at approximately 0.06 and 0.94. The dominant outcome was that the parent bubble breaks up into one large and one much smaller daughter bubble. The formation of two equally

sized daughter bubbles was only very rarely observed, but a very small increase in these events is apparent in the data for 30 °C. We note that the number of reliable events measured at 30 °C was relatively low (366, compared to approximately 1374 for 11 °C), making these data slightly noisier. The distributions of volume split ratios at different temperature were almost indistinguishable, strongly suggesting that the volume split ratio is independent of water viscosity.

B. Effects of surface tension on fragmentation

[Figure 6](#) shows the probability distributions of the volume split ratio for the three surface tension cases at 22 °C. The consistency of the average measured parent bubble radius (always 3.2 mm) for different values of surface tension was unexpected, since surface tension has been observed to affect pinch-off bubble size ([Czerski and Deane, 2010](#)), but our comparisons are more robust as a result.

The observed distributions are indistinguishable from those seen in the temperature experiments: a U-shaped distribution with maxima at approximately 0.06 and 0.94. There was no small local maximum for similarly-sized bubbles. The largest variations between distributions were again seen very close to the peaks. A more limited number of experiments were carried out at different pump speeds (30, 40 and 50 rpm) and analyzed using photography, and the volume split ratio again matched this pattern for all pump speeds (and therefore for all Weber numbers within the tested range).

C. PIV results

The average flow field and dissipation rate are shown in [Fig. 4](#). The flow pattern was not symmetrical, but the PIV was carried out after the majority of the bubble experiments, and this records the actual conditions during single phase flow in the same operating conditions. The asymmetry was due to the lower tube having a 2° deviation from vertical. The flow from the left hand tube (the higher of the two) dominated the flow field. This jet exhibited averaged velocities of approximately 0.6 m/s at a pump speed of 50 rpm and a vertical extent of approximately 2.2 cm. The regions of highest shear were close to the tube exits. The pulsed nature of the peristaltic pump was detectable in the velocity variation over time (which varied by up to a factor of 2), but cannot be seen in the averaged values.

In the region between the tubes, the time-averaged dissipation rates estimated using the LePIV method varied by up to 4 m²/s³. Time-averaged shear rates ranged from 16 to 62 s⁻¹ between the flow tubes. The maximum shear rate, calculated from Eq. (9), varied between 19 and 71 s⁻¹.

D. Locations of bubble fragmentation within the flow field

The photographic volume split ratio probability distributions matched the pattern shown in [Figs. 5\(c\)](#) and [Figure 6](#) for all pump speeds, temperatures and surface tensions. [Figure 7](#) shows the number of fragmentation events for all pump speeds, segregated by shear rate at the fragmentation location.

Bubble fragmentation events predominantly occurred at locations with maximum shear rates close to 20 s⁻¹. The distribution moves to the right as the pump speed increases, indicating that maximum shear rate alone cannot explain the fragmentation location and that spatial

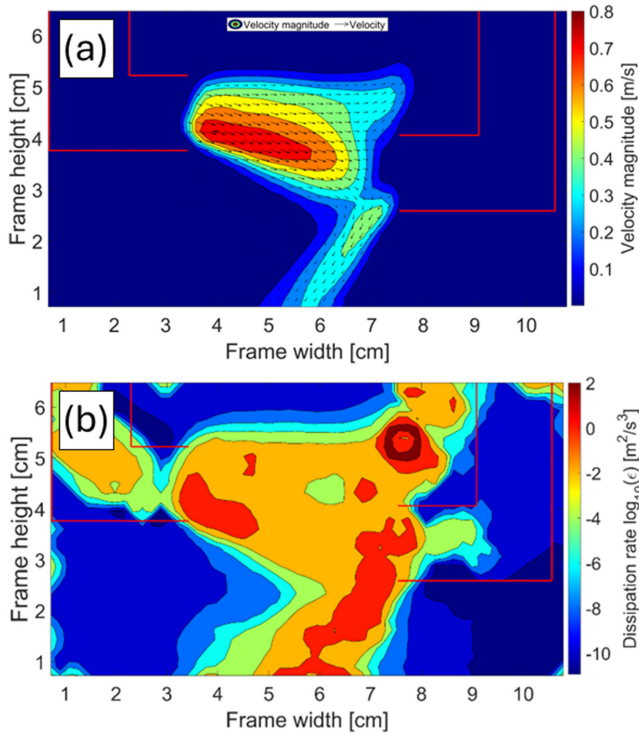


FIG. 4. (a) Averaged velocity magnitude for 50 rpm and 1 cm offset. Red lines show the glass tube positions and (b) dissipation rate for 50 rpm and 1 cm offset. Calculated using the LePIV method.

location relative to the flow tubes, turbulent eddies or previous deformation history may also matter.

The location of fragmentation was also checked at a lowered surface tension of 0.031 N/m and a pump speed of 30 rpm, and the volume split ratio was observed to be independent of the maximum shear rate at the location of fragmentation.

E. Bubble fragmentation type

The photographic data were used to categorize fragmentation events into the three types listed in Sec. II C: solo binary fragmentation, more than one fragmentation within the field of view, and multiple small bubbles produced in succession from one elongated filament. Figure 8 shows the proportion of event types at each pump speed and with lowered surface tension.

As the pump speed, and therefore, the dissipation rate and Weber number increase, the probability of successive fragmentations following on soon after the initial event increases significantly. The majority of events for all cases involved multiple fragmentation events in a cascade. The photographic data show that the fragmentation process at low surface tension is the same as at standard surface tension, although the rate of fragmentation is higher.

A representative dissipation rate for each measurement case was calculated by averaging over the dissipation rates in the box shown in Fig. 7, which corresponds to the region where most fragmentations occurred. Table I shows the measured parameters for each case. Note

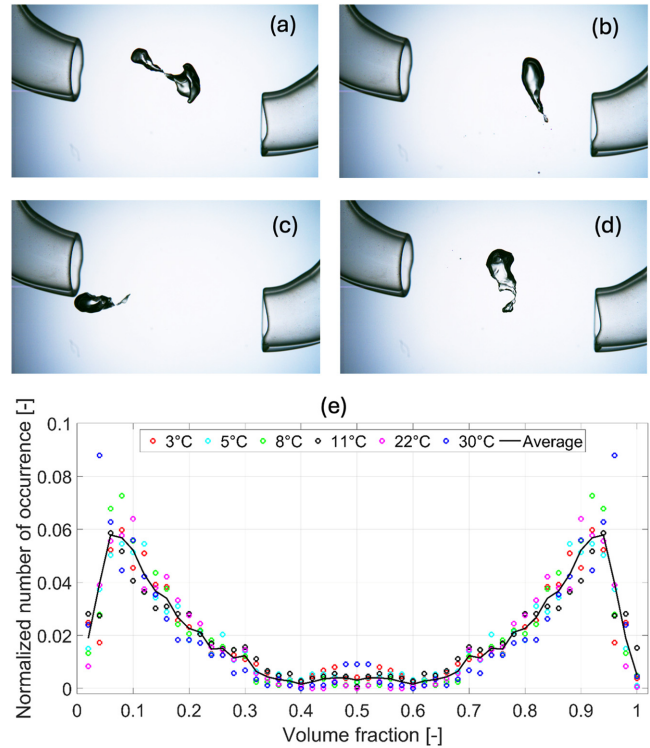


FIG. 5. Example fragmentation events with a volume split ratio of (a) 0.65:0.35, (b) 0.99:0.01, (c) 0.94:0.06, and (d) 0.93:0.07. The field of view is 4.5 × 8.0 cm for all images. (e): Normalized volume split ratio for all temperatures. The black solid line shows the average for all temperatures.

that the volume split ratio data shown in Figs. 5(c) and Figure 6 were collected at a pump speed of 50 rpm.

V. DISCUSSION

Figure 9 shows the averaged distribution across all 7 570 fragmentation events in all conditions. The results show considerable consistency and represent conditions with a Weber number of 2–5, and a

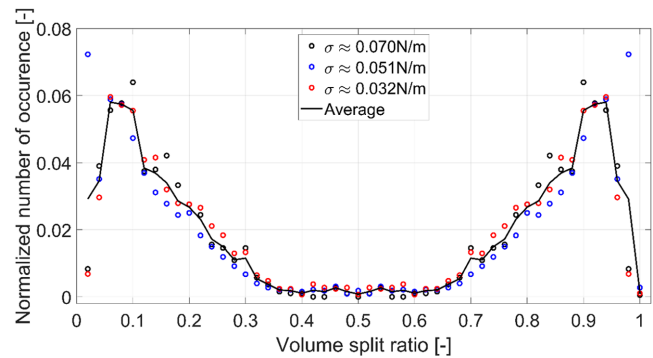


FIG. 6. Normalized volume split ratio for varying surface tension at 22 °C: 0.032 N/m (red circles), 0.051 N/m (blue circles), and 0.070 N/m (black circles). Black solid line shows the average for all surface tension values.

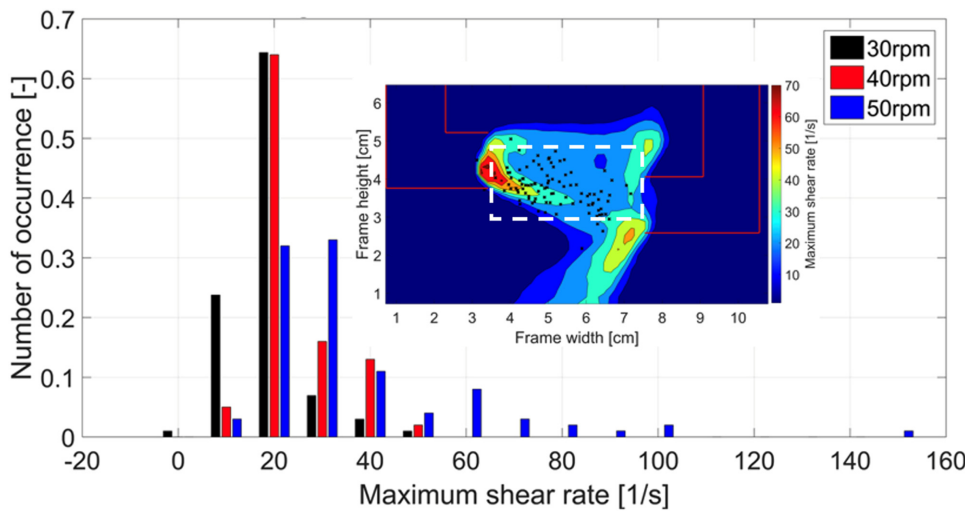


FIG. 7. Normalized number of fragmentation events for all pump speeds (black: 30 rpm, red: 40 rpm and blue: 50 rpm). Inset: field of maximum shear rate at 50 rpm with black crosses marking locations of fragmentation events. The representative turbulent dissipation rate shown in Table I is the mean value within the dashed white box.

ratio of parent bubble size to the Hinze scale of 1–2.3. We did not collect data for Weber numbers above 5.3. We are aware of one previous study, which directly measured the volume split ratio during fragmentation in turbulence (Vejražka et al., 2018), and Fig. 9 is broadly in line with their data, although our distribution shows features not seen in their study.

The peaks in the average probability density function for the volume split ratio are at 0.06 and 0.94, and we see a steep linear decline on the outer side of the peaks that has not previously been observed. Our acoustical method allowed the detection of bubbles with a volume of 0.013 of the original bubble volume. The radius of a small daughter bubble at the peak (where the volume split is 0.06:0.94) is 1.25 mm for a 3.2 mm radius parent bubble. These small bubbles are significantly smaller than the Hinze scale and do not fragment again. This distribution has three noteworthy features: the overall U-shape, the potential small rise at the center in some conditions, and the steep drop-off on either side.

It is not clear whether the steep drop-off is a real feature that was not detected in previous work, or an artifact caused by the measurement method. The only previous directly comparable measurements

were made by Vejražka et al. (2018), and they observed the greatest bubble number in the smallest bin, with a smooth increase towards the edge rather than a peak. Their measurements were made with photography (with the potential for bubble distortion and orientation to increase the uncertainty in the radius measurement), with a smaller sample size (1066 events in total).

It is expected that there will be a size cutoff for the smallest bubble that is likely to be created by a capillary-driven mechanism, based on the timescales and size scales of this type of instability. The sharp decline in the number of bubbles produced for volume split ratios below 0.06 and above 0.94 could, therefore, be related to limits set by capillary fragmentation on the thinnest neck that can form before a new bubble is created.

However, there is also a potential artifact that could be caused by the use of acoustics, because the acoustical method depends on detecting volume oscillations of the daughter bubbles just after the moment of fragmentation. Smaller bubbles have greater relative damping and so will oscillate for fewer cycles, potentially making them harder to detect, but we think that the balance of probabilities is that this is not a limiting factor here because the position of the peaks is the same in all

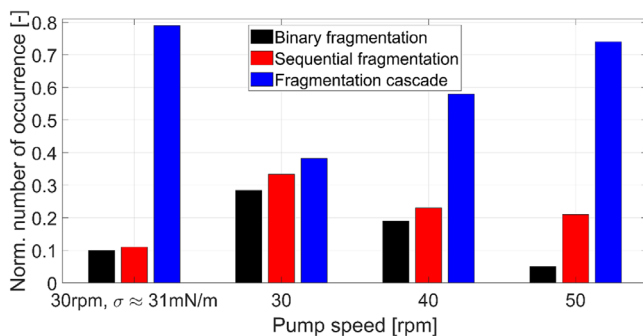


FIG. 8. Number of binary fragmentation events (black), sequential fragmentation events (red), and fragmentation cascades (blue) at varying pump speed and surface tension. Except for the set on the left, all these results are for clean water. The Weber numbers for these cases, from left to right, are 5.0, 2.3, 2.9, and 5.3.

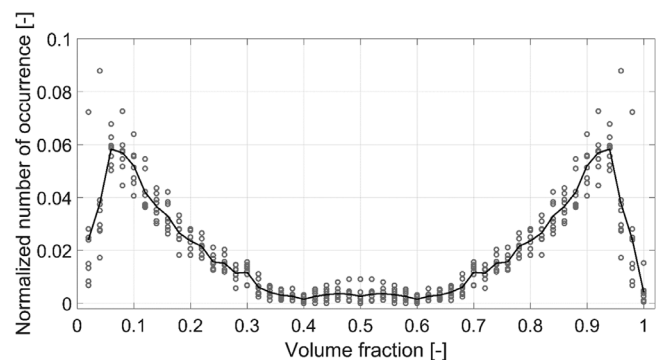


FIG. 9. Volume split ratio for all experiments. Each gray circle represents the normalized number in that bin for a different water condition, and the black solid line is the average over all experiments.

TABLE I. Characterization of the flow environment generated by different pump speeds, using the typical central values of flow characteristics. Hinze scales are calculated using $We_c = 3$.

Pump speed /rpm	Average shear rate	Max. shear rate	Dissipation rate	Weber number clean water	Hinze scale clean water	Weber number for $\sigma=0.03$ N/m	Hinze scale for $\sigma=0.03$ N/m
30	22 s^{-1}	27 s^{-1}	$0.22 \text{ m}^2/\text{s}^3$	2.2	3.8 mm	5.0	2.4 mm
40	27 s^{-1}	30 s^{-1}	$0.51 \text{ m}^2/\text{s}^3$	2.9	2.7 mm	8.8	1.7 mm
50	35 s^{-1}	40 s^{-1}	$0.83 \text{ m}^2/\text{s}^3$	5.3	2.3 mm	12.1	1.4 mm

conditions. It has previously been noted (Czerski and Deane, 2010) that the speed of the neck retraction driving the acoustical pulse during bubble pinch-off decreases as the surface tension decreases, making fragmentation events at lower surface tension quieter. Therefore, if the lack of a detectable signal was the cause of the drop-off, the peak position would be different for the measurements at lower surface tension, and this is not observed. We do not have enough evidence to fully resolve whether this drop-off is a feature or an artifact in this study.

If the peak is real, it may shed light on the smallest bubbles formed underneath breaking waves in different conditions, and the gas they inject into the ocean. Even in very high wind conditions in the open ocean (up to 28 m/s wind speed and 10 m significant wave height), observations have shown that bubbles with a radius greater than 200 μm are extremely rare even two meters beneath the surface (Czerski *et al.*, 2022). The plumes of bubbles carried to greater depths are much smaller than this (the peak volume contribution comes from bubbles 70–80 μm radius, and the smallest measured in that study were 20 μm radius). It is unknown whether these very small bubbles are predominantly formed at approximately this size near the surface and are quickly stabilized by surfactants, or whether they originally have a larger size and shrink due to dissolution. The full bubble size distribution formed at the surface, including the size of the very smallest bubbles originally created, is a critical piece of evidence needed to answer this question.

The U-shape and the possible central rise provide evidence for the mechanism of fragmentation. As described by Rivière *et al.*, (2022), two mechanisms appear to be responsible for the bubble size distribution under breaking waves, and the Rivière study separates them based on the timescale of the breakup. A slower eddy-driven mechanism can cause fragmentation into two approximately equally sized bubbles, and faster capillary instabilities in elongated filaments can cause the production of one sub-Hinze scale bubble and one much larger bubble. Rivière *et al.*, (2022) considered the origin of such filaments to be an eddy-driven breakup, where long filaments are formed as the equally sized daughter bubbles separate, and then subsequently fragment further. However, our data show that an initial fragmentation is not required to generate these elongated filaments, and so the capillary-driven “splitting” mechanism can operate in the absence of the eddy-driven “breakup” mechanism. The presence of a small bump in the center of the volume split ratio distribution is evidence for the occasional operation of an eddy-driven mechanism, but this was a small minority of cases. It is not clear whether the formation of an elongated neck without prior breakup is related to the flow configuration used here, with offset jets and a significant average shear in the background of the turbulence, or whether it could happen in the absence of that background shear pattern. Vejražka *et al.* (2018) also used jets to

generate turbulence in their experiments and saw a similar pattern of results.

Although our experiments were not conducted in perfectly isotropic homogenous turbulence, this does not necessarily invalidate our conclusions relating to the situation underneath breaking waves. The fluid flow underneath breaking waves is also not isotropic and homogenous, although most bubble fragmentation studies consider this ideal case. The rotation underneath a breaking wave (Deane and Stokes, 2002) generates regions of shear combined with turbulence, which may affect bubble breakup in the same way as the shear in our experiments.

The fragmentation rates of 33%–66% suggest that the parent bubbles in our experiments were very close to the Hinze scale (since the Hinze scale is commonly considered the size at which half the bubbles fragment). This is backed up by the data in Table I, showing that the ratio of the parent bubble radius to the Hinze scale for the measured dissipation rate varied between 1 and 2.2. Rivière *et al.* (2022) suggested that the formation of elongated filaments only happens for bubbles that are significantly larger than the Hinze scale. Their numerical simulations cover ratios of the parent bubble diameters to the Hinze scale of 2.9–5.2. However, our data show frequent formation of elongated filaments for bubbles, which are very close to the Hinze scale, at a ratio of 1:1. The Weber number in our experiments was a maximum of 5.3, in contrast to $We = 100$, in the Rivière experiments. The data of Vejražka *et al.* (2018) also show very few fragmentations producing equally sized bubbles for low Weber numbers. There is, therefore, ample evidence for the “splitting” mechanism operating for parent bubbles that are very close to the Hinze scale in size. The implication is that either regions of overlaid shear are important for generating elongated filaments, which can fragment due to capillary instability, or that the elongated filaments can form for bubbles as small as the Hinze scale even in isotropic turbulence and do not require a prior fragmentation. This suggests that the exact configuration of the breaking wave could have a significant impact on the number of small bubbles generated, if it changes the overall mean shear pattern in the flow.

Our data only applied to the bubble size distribution produced by the first fragmentation event and does not consider the influence of fragmentation rate. As expected, the fragmentation rate increased at higher Weber numbers. The greater the dissipation rate, the greater the probability of multiple small bubbles being created from the same long neck on a deformed bubble, consistent with Vejražka *et al.* (2018).

Several studies have addressed the question of whether bubble size distributions under breaking waves are independent of temperature, e.g., (Asher and Farley, 1995; Slauenwhite and Johnson, 1999). Callaghan *et al.* (2014) found that the temperature-related changes in the bubble size distribution produced in a Marine Aerosol Reference

Tank were mostly observed in bubbles greater than $670\ \mu\text{m}$ in radius. However, Salter *et al.* (2014) observed a factor of 20 variation in the bubble number at the smallest bubble sizes between temperatures of -1.3 and $30.1\ ^\circ\text{C}$ from a plunging jet, with more bubbles at the colder temperatures. Our results suggest that any variation in the small bubble size distribution with temperature is not due to changes in the volume split ratio at fragmentation, which leaves either viscosity-dependent features of the flow pattern or the fragmentation rate as possible explanations.

VI. CONCLUSIONS

We have measured the volume split ratio probabilities in detail for bubbles fragmenting in sheared and turbulent flow, using acoustical methods, which produce a large dataset very efficiently. The dominant outcome is the formation of one very large daughter bubble and one very small one. We observed strong narrow peaks in the probability density function at volume split ratios of 0.06 and 0.94, with a steep linear decline on the outside of each peak, and extremely low values in between the two peaks. The observed probability density function and the peak positions were independent of temperature and surface tension (over a range of $3\ ^\circ\text{C}$ to $30\ ^\circ\text{C}$, and 0.032 – $0.072\ \text{N/m}$). At a water temperature of $30\ ^\circ\text{C}$, a small additional increase in probability (maximum height $\sim 15\%$ of the main peaks) was observed for the case of equally-sized bubbles.

High speed photography confirmed that the predominant fragmentation mechanism was the stretching of an approximately Hinze-scale sized bubble to form a long thin filament at one end, followed by a daughter bubble fragmenting from the end of the filament. In some cases (particularly at higher Weber numbers, ~ 5), within a few milliseconds, further small bubbles were likely to fragment from the same filament. This matches the description of capillary-driven fragmentation, described in Rivière *et al.*, (2022), although we observed this mechanism operating for bubbles very close to the Hinze scale, and for Weber numbers as low as 2, far lower than previously suggested.

We saw elongated filaments form purely as a result of bubble deformation in the flow, in contrast to Rivière *et al.*, (2022) who found that these filaments are the result of a previous breakup into approximately equally sized bubbles (and therefore require a larger initial bubble). Our experiments used offset jets to generate the turbulence, and so there was an underlying shear pattern superimposed on the turbulence, and this may be responsible for the elongated filament formation. Our results imply that either regions of overlaid mean shear are important for generating elongated filaments, which can fragment due to capillary instability, or that the elongated filaments can form for bubbles as small as the Hinze scale even in isotropic turbulence and do not require a prior fragmentation. In the first case, this would suggest that underneath a breaking wave, the mean shear patterns may also be important for determining the presence and size distribution of sub-Hinze scale bubbles (because they determine the extent of filament formation for near-Hinze scale bubbles). So future studies may need to go beyond isotropic homogenous turbulence and consider the full flow geometry.

The acoustical method used here to measure the sizes of the daughter bubbles has been shown to be very effective at producing sufficient quantities of data for robust statistical analysis. Thousands of cases can be analyzed relatively quickly, removing the need for complex image processing or manual assessment of images. Future studies of fragmentation rate, as well as further exploration of the effect of the

water conditions on fragmentation outcome for different bubble sizes, would benefit from this method.

ACKNOWLEDGMENTS

The authors would like to acknowledge funding from HC's fellowship from the UK Natural Environment Research Council NE/H016856/1, and UD's Ph.D. fellowship from the Department of Mechanical Engineering at University College London.

AUTHOR DECLARATIONS

Conflict of Interest

The authors have no conflicts to disclose.

Author Contributions

Ulrike Drähne: Formal analysis (lead); Investigation (lead); Writing – original draft (equal); Writing – review & editing (supporting). **Andrea Ducci:** Conceptualization (supporting); Methodology (equal); Supervision (equal); Writing – review & editing (equal). **Helen Czerski:** Conceptualization (lead); Methodology (equal); Supervision (equal); Writing – original draft (equal); Writing – review & editing (equal).

DATA AVAILABILITY

The bubble data used for this study will be available in the UCL Data Repository. We will link to this paper when the final data are deposited there (we cannot change the record without changing the DOI, so we need to know the DOI for the paper before final deposition), so we provide an intermediate private link to the data here: <https://doi.org/10.6084/m9.figshare.25436332.v1> These data will be published under a CC BY-NC-SA 4.0 license once this paper is in its final form.

REFERENCES

- Asher, W. E. and Farley, P. J., "Phase-Doppler anemometer measurement of bubble concentrations in laboratory-simulated breaking waves," *J. Geophys. Res.* **100**(C4), 7045–7056, <https://doi.org/10.1029/95JC00068> (1995).
- Berny, A., Deike, L., Séon, T., and Popinet, S., "Role of all jet drops in mass transfer from bursting bubbles," *Phys. Rev. Fluids* **5**(3), 033605 (2020).
- Buffo, M. M., Corrêa, L. J., Esperança, M. N., Cruz, A. J. G., Farinas, C. S., and Badino, A. C., "Influence of dual-impeller type and configuration on oxygen transfer, power consumption, and shear rate in a stirred tank bioreactor," *Biochem. Eng. J.* **114**, 130–139 (2016).
- Callaghan, A. H., Stokes, M. D., and Deane, G. B., "The effect of water temperature on air entrainment, bubble plumes, and surface foam in a laboratory breaking-wave analog," *J. Geophys. Res.* **119**(11), 7463–7482, <https://doi.org/10.1002/2014jc010351> (2014).
- Chua, G., Chitre, M., and Deane, G. B., "Long-lived bubbles and their impact on underwater acoustic communication," *IEEE J. Oceanic Eng.* **46**(3), 1008–1023 (2021).
- Czerski, H., Brooks, I. M., Gunn, S., Pascal, R., Matei, A., and Blomquist, B., "Ocean bubbles under high wind conditions – Part 2: Bubble size distributions and implications for models of bubble dynamics," *Ocean Sci.* **18**(3), 587–608 (2022).
- Czerski, H. and Deane, G. B., "Contributions to the acoustic excitation of bubbles released from a nozzle," *J. Acoust. Soc. Am.* **128**(5), 2625–2634 (2010).
- Czerski, H. and Deane, G. B., "The effect of coupling on bubble fragmentation acoustics," *J. Acoust. Soc. Am.* **129**(1), 74–84 (2011).

- de Jong, J., Cao, L., Woodward, S. H., Salazar, J. P. L. C., Collins, L. R., and Meng, H., "Dissipation rate estimation from PIV in zero-mean isotropic turbulence," *Exp. Fluids* **46**(3), 499–515 (2008).
- de Leeuw, G., Andreas, E. L., Anguelova, M. D., Fairall, C. W., Lewis, E. R., O'Dowd, C., and Schwartz, S. E., "Production flux of sea spray aerosol," *Rev. Geophys.* **49**(2), RG2001, <https://doi.org/10.1029/2010rg000349> (2011).
- Deane, G. B., "Surface tension effects in breaking wave noise," *J. Acoust. Soc. Am.* **132**(2), 700–708 (2012).
- Deane, G. B., "The performance of high-frequency doppler sonars in actively breaking wave crests," *IEEE J. Oceanic Eng.* **41**(4), 1028–1034 (2016).
- Deane, G. B. and Czerski, H., "A mechanism stimulating sound production from air bubbles released from a nozzle," *J. Acoust. Soc. Am.* **123**(6), EL126–132 (2008).
- Deane, G. B. and Stokes, D. M., "Scale dependence of bubble creation mechanisms in breaking waves," *Nature* **418**, 839 (2002).
- Deane, G. B. and Stokes, M. D., "Model calculations of the underwater noise of breaking waves and comparison with experiment," *J. Acoust. Soc. Am.* **127**(6), 3394–3410 (2010).
- Deane, G. B., Stokes, M. D., and Callaghan, A. H., "The saturation of fluid turbulence in breaking laboratory waves and implications for whitecaps," *J. Phys. Oceanogr.* **46**(3), 975–992 (2016).
- Deike, L., "Mass transfer at the ocean–atmosphere interface: The role of wave breaking, droplets, and bubbles," *Annu. Rev. Fluid Mech.* **54**(1), 191–224 (2022).
- Deike, L. and Melville, W. K., "Gas transfer by breaking waves," *Geophys. Res. Lett.* **45**(19), 10,482–41,049, <https://doi.org/10.1029/2018gl078758> (2018).
- Ducci, A. and Weheliye, W. H., "Orbitally shaken bioreactors–viscosity effects on flow characteristics," *AIChE J.* **60**(11), 3951–3968 (2014).
- Garrett, C., Li, M., and Farmer, D. M., "The connection between bubble size spectra and energy dissipation rates in the upper ocean," *J. Phys. Oceanogr.* **30**(9), 2163–2171 (2000).
- Leroy, V., Devaud, M., and Bacri, J.-C., "The air bubble: Experiments on an unusual harmonic oscillator," *Am. J. Phys.* **70**, 1012–1019 (2002).
- Martínez-Bazán, C., Montañés, J. L., and Lasheras, J. C., "On the breakup of an air bubble injected into a fully developed turbulent flow. Part 2. Size PDF of the resulting daughter bubbles," *J. Fluid Mech.* **401**, 183–207 (1999).
- Minnaert, M., "On musical air-bubbles and the sounds of running water," *London, Edinburgh, Dublin Philos. Mag. J. Sci.* **16**(14), 235–248 (1933).
- Qi, Y., Mohammad Masuk, A. U., and Ni, R., "Towards a model of bubble breakup in turbulence through experimental constraints," *Int. J. Multiphase Flow* **132**, 103397 (2020).
- Qi, Y., Tan, S., Corbitt, N., Urbanik, C., Salibindla, A. K. R., and Ni, R., "Fragmentation in turbulence by small eddies," *Nat. Commun.* **13**(1), 469 (2022).
- Rivière, A., Mostert, W., Perrard, S., and Deike, L., "Sub-Hinze scale bubble production in turbulent bubble break-up," *J. Fluid Mech.* **917**, A40 (2021).
- Rivière, A., Ruth, D. J., Mostert, W., Deike, L., and Perrard, S., "Capillary driven fragmentation of large gas bubbles in turbulence," *Phys. Rev. Fluids* **7**(8), 083602 (2022).
- Rodriguez, G., "An engineering characterisation of shaken bioreactors: Flow, mixing and suspension dynamics," Doctoral thesis (University College London, 2017).
- Rosti, M. E., Ge, Z., Jain, S. S., Dodd, M. S., and Brandt, L., "Droplets in homogeneous shear turbulence," *J. Fluid Mech.* **876**, 962–984 (2019).
- Salisbury, D. J., Anguelova, M. D., and Brooks, I. M., "On the variability of whitecap fraction using satellite-based observations," *J. Geophys. Res. Oceans* **118**(11), 6201–6222, <https://doi.org/10.1002/2013JC008797> (2013).
- Salter, M. E., Nilsson, E. D., Butcher, A., and Bilde, M., "On the seawater temperature dependence of the sea spray aerosol generated by a continuous plunging jet," *J. Geophys. Res.* **119**(14), 9052–9072, <https://doi.org/10.1002/2013jd021376> (2014).
- Sheng, J., Meng, H., and Fox, R. O., "A large eddy PIV method for turbulence dissipation rate estimation," *Chem. Eng. Sci.* **55**, 4423–4434 (2000).
- Slauenwhite, D. E. and Johnson, B. D., "Bubble shattering: Differences in bubble formation in fresh and salt water," *J. Geophysical Res.* **104**, 3265–3275 (1999).
- Stramski, D. and Tegowski, J., "Effects of intermittent entrainment of air bubbles by breaking wind waves on ocean reflectance and underwater light field," *J. Geophysical Res.* **106**, 31345–31360 (2001).
- Tsouris, C. and Tavlarides, L. L., "Breakage and coalescence models for drops in turbulent dispersions," *AIChE J.* **40**, 395–406 (1994).
- Vejražka, J., Zedníková, M., and Stanovský, P., "Experiments on breakup of bubbles in a turbulent flow," *AIChE J.* **64**(2), 740–757 (2018).
- Wang, T., Wang, J., and Jin, Y., "A novel theoretical breakup kernel function for bubbles/droplets in a turbulent flow," *Chem. Eng. Sci.* **58**(20), 4629–4637 (2003).
- Wanninkhof, R., "Relationship between wind speed and gas exchange over the ocean revisited," *Limnol. Ocean. Methods* **12**(6), 351–362 (2014).
- Wurl, O., Miller, L., and Vagle, S., "Production and fate of transparent exopolymer particles in the ocean," *J. Geophys. Res.* **116**, C00H13, <https://doi.org/10.1029/2011JC007342> (2011).